

Accepted Manuscript

Methane transport through hierarchical silica micro-mesoporous materials: From non-equilibrium atomistic simulations to phenomenological correlations

Anh Phan, Alberto Striolo



PII: S1387-1811(19)30402-0

DOI: <https://doi.org/10.1016/j.micromeso.2019.06.021>

Reference: MICMAT 9559

To appear in: *Microporous and Mesoporous Materials*

Received Date: 20 February 2019

Revised Date: 4 June 2019

Accepted Date: 17 June 2019

Please cite this article as: A. Phan, A. Striolo, Methane transport through hierarchical silica micro-mesoporous materials: From non-equilibrium atomistic simulations to phenomenological correlations, *Microporous and Mesoporous Materials* (2019), doi: <https://doi.org/10.1016/j.micromeso.2019.06.021>.

This is a PDF file of an unedited manuscript that has been accepted for publication. As a service to our customers we are providing this early version of the manuscript. The manuscript will undergo copyediting, typesetting, and review of the resulting proof before it is published in its final form. Please note that during the production process errors may be discovered which could affect the content, and all legal disclaimers that apply to the journal pertain.

Methane Transport through Hierarchical Silica Micro-Mesoporous Materials: From Non-Equilibrium Atomistic Simulations to Phenomenological Correlations

Anh Phan¹ and Alberto Striolo¹

¹Department of Chemical Engineering, University College London, London, WC1E 7JE, UK

Abstract

Atomistic non-equilibrium molecular dynamics simulations were employed to quantify methane transport in hierarchical porous networks. Model amorphous silica materials were used as solid substrates, which allows us to construct pore networks with well-defined properties. The results show that the methane diffusivity and permeability through the pores strongly depend on the frameworks. Analysis of the vector fields for methane within the pores reveals the existence of local back-flow near the solid substrates, which disturbs methane transport. Varying the pore cross-sectional areas leads to changes in the entropy potential along the flow direction, which influences the molecular path length. The results show a linear relationship between methane transport (i.e., permeability) and a pore characteristic parameter that takes into consideration porosity, constriction factor, and tortuosity. This relation holds for hierarchical porous materials containing both micropores and mesopores. Diffusivity and permeability of methane through porous media are found to scale as a power function of porosity and constriction factor. These are measurable descriptors, suggesting that transport properties could be predicted for engineering and natural materials once characterisation data are available. For example, we show here that a power law can describe results obtained for Fontainebleau sandstone. The good agreement achieved suggests that using the approach presented not only enables the quantification of molecular effects influencing fluid transport, but also yields the reliable prediction of diffusivity and permeability of fluids through sedimentary rocks using as sole input macroscopic pore structure information.

Keywords: molecular simulations, amorphous silica, transport diffusivity, permeability, tortuosity

1. Introduction

Shale gas has received much attention in recent years due to depletion of conventional resources, as well as several scientific and technological challenges faced to achieve high production with minimal environmental impact. One challenge in the field is bridging fluid dynamic observations within nanometer pores in kerogen to entire shale gas reservoirs simulations [1]. Shale matrices are structurally complex natural porous media whose pore space is highly heterogeneous, with a pore distribution spanning orders of magnitude, from a few nanometres to a few microns [2]. A fundamental understanding of fluid transport in shale matrices during shale gas extraction is important for improving gas production and lowering both production costs and environmental footprint. Such understanding remains an important challenge in this field.

The fluid flow through shale reservoirs is a complex, multi-scale phenomenon because of a combination of phenomena including adsorption, desorption, surface diffusion along pore walls, convection (Darcy flow) and Knudsen diffusion through open pore spaces [3]. Many experimental and theoretical efforts have been carried out to understand the relationship between the morphology of porous materials and the relevant transport properties [4-6]. For example, Reich et al. [4, 5] employed a reconstruction-simulation approach to quantify the impact of degree of heterogeneity and packing-scale order on hindered diffusion in mesoporous silica. Micropores, if present, can dominate overall diffusion behaviour compared to mesopores. The geometry of the micropores plays a significant role in controlling the amount of fluids that cross or enter a natural porous media [7-9]. In small nanopores such as those commonly found in shale matrices, fluid flow is not expected to be described by Darcy-type expressions, as the transport mechanisms associated with pore-wall interactions become dominant and continuum descriptions break down [10]. While many atomistic simulation studies have been conducted to quantify structure-transport properties for fluids confined in single pores [11], describing gas transport properties remains challenging due to the presence of multi-scale porous characteristics and compositional heterogeneity within the rocks. The challenge consists in up-scaling the simulation results obtained in a single pore, to predict fluid transport through a matrix, as pore-edge effects, preferential pathways and many other phenomena can affect the results. Permeability

through shales can be measured experimentally [12]. For example, Bhandari et al. [13] reported permeability as low as 2 nanodarcy, and anisotropy of 40 (ratio between permeability measured in two directions) for their samples, which consisted of 4% total organic content and contained large amounts of quartz, calcite, and clay. Measured shale permeability ranges from 0.1 to 1000 nanodarcy [12, 14], and anisotropy from as little as 5 to 10000 or more [12, 15]. Starting from these experimental data, research has focussed on reconstructing three-dimensional volumes to map the pore space distribution and simulate permeability using, e.g., the Lattice Boltzmann Method [3, 16-18], stochastic modelling [19], or a combination of the Metropolis-Hastings and genetic algorithms [20]. At the smallest length scale, molecular dynamics (MD) simulations have become an efficient tool for studying the impacts of confinement on fluid properties and calculating transport coefficients for use in multi-scale models of fluid flow [21-25], although in general limited by the available computing resources. Both equilibrium and non-equilibrium MD methods have been widely implemented to estimate transport diffusivity and permeability for fluids through a porous network [24, 26-30]. Among these methods, the boundary-driven non-equilibrium MD (BD-NEMD) has revealed potential of an effective computational approach for correctly determining transport diffusivity as well as permeability, which enables us to consider explicitly the effect of adsorption of the fluid molecules on the pore walls [28, 31].

In this study, we employ the BD-NEMD approach to simulate methane flow through hierarchical amorphous silica porous materials representative of those found in shale gas plays. The model materials were constructed as a simplified representation of shale matrixes. In shale rocks, small amount of organic material (kerogen) is dispersed within large matrixes of various minerals, some of which can be siliceous [13, 14]. By applying the simulations on ‘synthetic’ model porous materials, we collect results for permeability and diffusivity, and we correlate such results with pore structure information. To estimate the fluid diffusivity through a porous medium, empirical correlations have been proposed that predict deviations compared to bulk fluid properties, as well as theoretical models based on oversimplified pore geometry [32, 33]. Recently, for example, Hlushkou and Tallarek proposed an analytical formula involving three-point microstructural parameter and porosity for effective diffusivity prediction based on a number of physically reconstructed packed beds of fully

porous and core-shell particles [34]. In most cases, it is customary to divide the diffusivity in three factors: the void space in the porous medium, the average path length available across the medium, and the shrinkage in the effective flow because of changes in the pore cross-section [35, 36]. Three macroscopic descriptors follow: porosity, tortuosity, and constriction factor. Because tortuosity cannot be measured directly, it has been attempted to estimate it from porosity [37, 38]. The constriction factor is important when the fluid molecules have size comparable to the pore size [37, 39], which is the case for shale rocks.

In this study, we use simulation results to first correlate tortuosity with both porosity and constriction factor, and then we derive a quantitative relation between fluid transport and pore structure parameters that can be obtained once experimental data are available for a pore network. The empirical relation proposed for estimating diffusivity and permeability could have important implications for understanding structure-transport relations, but also for predicting fluid transport in shale reservoirs.

2. Simulation Methodology

Pore Models. We built model hierarchical porous media from amorphous silica. The models for hydroxylated amorphous silica surfaces were taken from those published by Ugliengo et al. [40] This group prepared bulk amorphous silica by conducting classic molecular dynamics simulations starting from the configuration of bulk β -cristobalite. They heated this structure at 6000 K, and then they cooled it to 300 K, so that the crystalline nature of silica was lost. To generate a realistic surface for amorphous silica, they extracted a slab of thickness 1.5 nm from the bulk, and they saturated the surface Si/SiO dangling bonds with OH groups that represented single silanol SiOH and germinal silanol Si(OH)₂ groups. Surface siloxane groups or Si – O – Si bridges with oxygen atoms are also present on the model SiO₂ surface [40]. To obtain the hydroxylated surface with 4.5 OH nm⁻², which mimics an experimental silica sample, they then performed dehydration by condensing the closest next-neighbouring pairs of H-bonded hydroxyl groups. The final structure was fully optimized using electronic density functional theory (DFT) calculations at the B3LYP/6-31G(d,p) level of theory [40].

To build our model materials, we used the $1.34 \times 1.34 \times 1.5 \text{ nm}^3$ hydroxylated amorphous silica substrate taken from Ugliengo et al. [40] as a unit cell. Within a unit cell, the distributions of surface atoms and silanol groups are random. The unit cell obtained from this reference is periodic in X and Y directions, and it was adapted for our system.

From the amorphous silica just described, we constructed hierarchically ordered micro-mesoporous materials that presented inter-connectivity between two domains [41, 42], including both micro- ($0.4 - 1.1 \text{ nm}$) and meso-porosities ($\sim 3.8 \text{ nm}$) [43], as illustrated in **Figure 1** and **Figure S1** in Supporting Information (SI). We built ten model systems. Details about the geometry of each model systems are shown in **Figure S1** in SI. The heterogeneity length scale of the synthetic systems considered here is within the scope of micro-mesoporous solid media [43].

We duplicate the unit-cell to create two parallel silica slabs and blocks A and B. The periodicity in surface functional groups is generated due to the duplication of the unit cells of our amorphous material. Two parallel silica slabs, which yield a slit-shaped mesopore, have X and Y dimensions of $L_{x,p} = 12.048 \text{ nm}$ and $L_{y,p} = 3.986 \text{ nm}$. Within this mesopore we placed blocks A and B at different locations to create pore networks. The X, Y and Z dimensions for the silica blocks A and B were $4.014 \times 3.986 \times 1.5$ and $2.677 \times 3.986 \times 1.5 \text{ nm}^3$, respectively. We saturated the pore edges with OH groups to achieve the surface density of OH groups (4.5 OH nm^{-2}) consistent with experiments. No DFT calculations were performed in the present study.

The pore networks are classified within three general groups (**Figure 1**, panel B): (1) Three pore networks in Group I have absolute porosity 0.61 ($\phi_1 = 0.61$), and they consist of 2 silica slabs and 2 blocks A (top). The position of the A blocks varied in these pore networks. (2) Six pore networks in Group II have absolute porosity 0.53 ($\phi_2 = 0.53$), and they consist of 2 silica slabs, 2 blocks A, and 1 block B (middle). (3) One pore network in Group III (bottom) is composed of 2 silica slabs and 4 blocks B, yielding absolute porosity 0.53 ($\phi_2 = 0.53$).

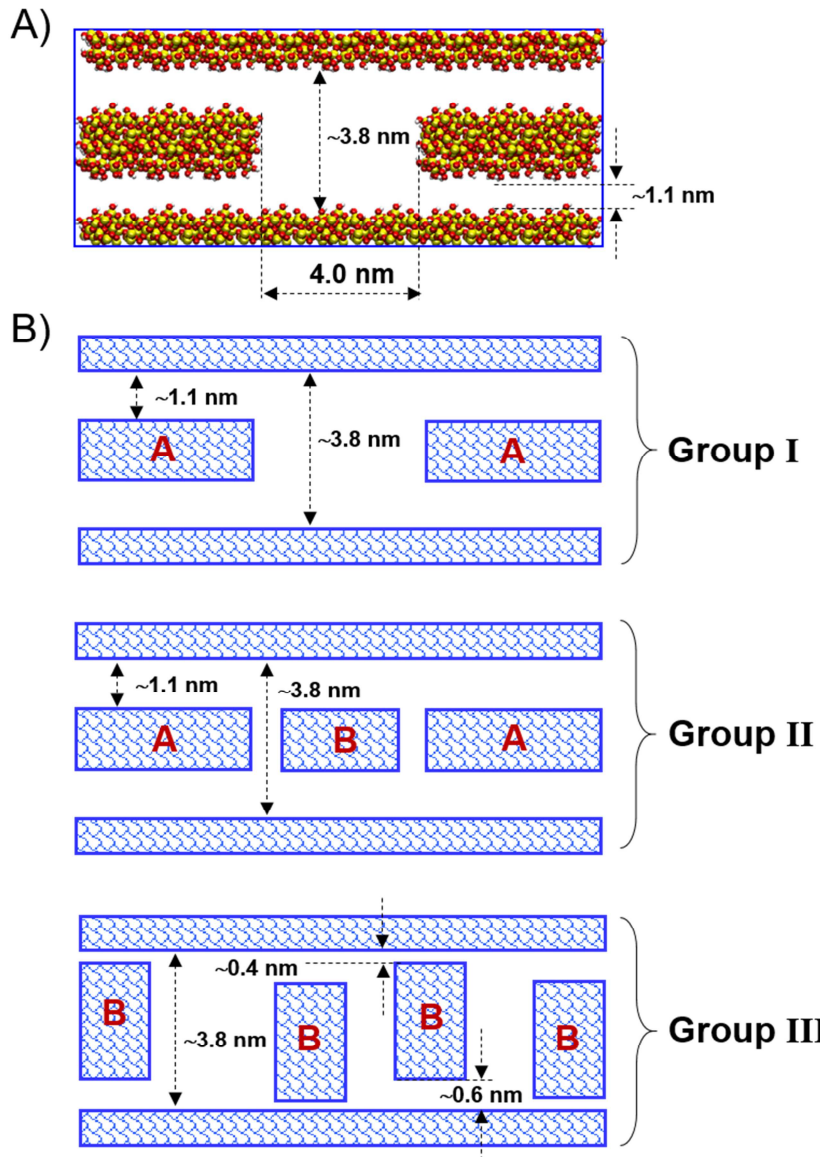


Figure 1. (A) Representative geometry of hierarchical amorphous silica porous materials consisting of both micropores ($\sim 0.4 - 1.1$ nm) and mesopores (~ 3.8 nm). Yellow, red and white spheres represent silicon, oxygen and hydrogen atoms, respectively. (B) Schematic illustration of various hierarchical porous media classified within three general groups: (1) three pore networks in Group I with porosity 0.61 and 2 blocks A (top), six pore networks in Group II with porosity 0.53 and two blocks A and one block B (middle) and 1 pore network in Group III with porosity 0.53 and 4 blocks B (bottom).

Force Fields. The CLAYFF force field was implemented to simulate the amorphous silica substrates [44]. Silicon and oxygen atoms were tethered to their initial positions by applying a harmonic restraint force with a spring constant of 100 kcal/mol. \AA . The surface hydroxyl hydrogen atoms were allowed to vibrate. The transferable potentials for phase equilibria (TraPPE) force field

was implemented to model methane [45]. Nonbonded interactions were modelled by means of dispersive and electrostatic forces. The electrostatic interactions were modelled by the Coulombic potential, with long-range corrections treated using the particle–particle particle–mesh (PPPM) method [46]. Dispersive interactions were modelled by 12–6 Lennard-Jones (LJ) potentials. The LJ parameters for unlike interactions were determined by Lorentz–Berthelot combining rules from the values of like components [47]. The cutoff distance for all interactions was set to 12 Å.

Simulation Setup. The simulation box is periodic in the three directions. The Y dimension of the simulation boxes (3.986 nm) reflects the periodicity of the silica solid substrates; the X and Z dimensions were set to 24.166 – 5.521 nm, respectively, for all the pore model systems. Due to periodic boundary conditions, the pore models are effectively infinite along the Y direction. Conversely, the pore models are finite along the X direction, along which they are exposed to feed (right in **Figure 2**) and permeate (left) phases.

Algorithms. We implemented the BD-NEMD method [28] to establish and maintain a constant pressure difference across the pore networks, and hence maintain a steady molar flux across the hierarchical porous media. We initially equilibrated the porous materials in the presence of methane for 20 ns, without applying any external force. The number of methane molecules ranged from 2000 to 2060 for each model system to ensure that the bulk pressure outside the pore models is ~ 20 MPa at equilibrium. Once equilibrium was achieved, we characterised the properties of the system (e.g., via quantifying density profiles for methane within the various pores in the networks).

We then carried out the BD-NEMD simulations by applying a force along the X-axis, acting in the direction of the arrow shown in **Figure 2**, top panel, to all methane molecules located in a thin slab (shaded region) of width $d_{ext} = 20$ Å of the permeate. In each BD-NEMD simulation, 20 ns of simulations were required to reach steady states. After this, production simulations were conducted for 20 – 140 ns. During equilibration, convergence to steady state is evaluated by examining the variations in the energy and temperature of the various systems, as well as the methane density profiles along the pores.

Implementation. Equilibrium and nonequilibrium MD simulations were conducted using the package GROMACS [48, 49] and LAMMPS [50], respectively. Simulations were performed in the

canonical ensemble (NVT), where the number of particles (N), the simulation volume (V), and the temperature (T) are kept constant. The equations of motion were solved by implementing the leapfrog algorithm[51] with 1.0 fs time steps. The simulated temperature was maintained at 338 K by a Nosé-Hoover thermostat [52, 53] with a relaxation time of 100 fs. We applied separate Nosé-Hoover thermostats to methane and to the atoms in the amorphous silica [54, 55] to reduce the perturbations on the dynamics of the system, since the system is exposed to a constant energy input due to the application of the external force on methane. He et al. [31] recently performed six temperature control schemes for BD-NEMD simulations to study methane transport in montmorillonite nanopores and reported that applying separate thermostats to the fluid particles and pore wall atoms yields excellent temperature control even for large applied forces.

3. Results and Discussion

Fluid Density Profiles at Equilibrium and During Flow. In **Figure 2** we show one simulation snapshot (top panel) and the density profile (bottom panel) for methane distributed along the length of the simulation box in the X direction when the applied external force is 0.05 kcal/(mol.Å). The results are shown for one pore network in Group *I* (system 1). The results show that the external force, which is applied to the methane molecules located in a thin slab (shaded region) (see **Figure 2**), yields a pressurised zone on the right of the porous media, within which an increase in methane density is observed. This is the ‘retentate’ volume. This external field is considered equivalent to imposing a density (or a pressure) gradient, leading to a macroscopic flux in the direction of the arrow in **Figure 2**. Under conditions of macroscopic density gradient, each methane molecule is more likely to diffuse from the higher density to lower density side, and the flow develops through the pores to the ‘eluate’ volume on the left of the pore network. A moderate external force yields a moderate perturbation to the simulated fluid, in correspondence to which the methane density in both bulk regions to the left and to the right of the pore network remains constant. Once steady states are achieved, the resultant methane density profile inside the network shows a wavelike pattern similar to the one observed during equilibrium simulations, when no external force is applied (see **Figure 3**, panel A). In **Figure 3**, panel B we report the in-plane density distributions of methane within layers closest to the bottom

(left) and top (right) silica slabs at equilibrium (top) and during flow (bottom) for system 1. Our analysis reveals that the positions of the high-density regions where methane molecules prefer to reside in equilibrium simulations are similar to those occupied preferentially when external forces are applied. These high methane density regions correspond to the locations of peaks of the wave as shown in Figure 3, panel A. This suggests that the external forces considered do not perturb strongly the structural properties of confined methane. However, once flow is induced, the density profiles show a decreasing gradient from the retentate (right) to the eluate volumes (left).

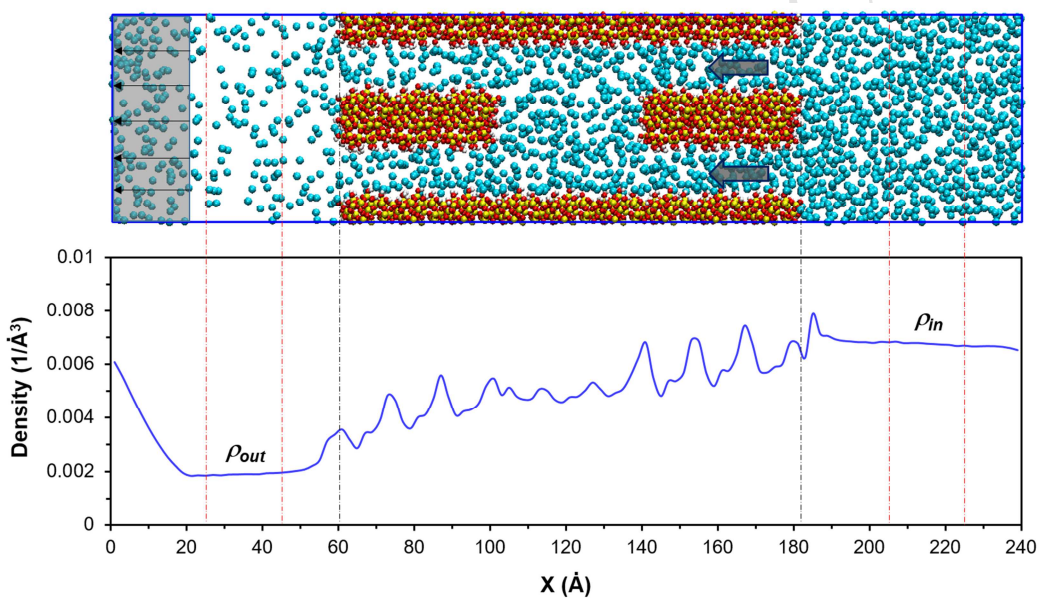


Figure 2. Top: Representative simulation snapshots for the final configuration of methane moving across the pore network in Group *I* (system 1) at 338 K. An external force of 0.05 kcal/mol. \AA is applied to methane molecules (cyan spheres) in the shaded region to drive flow through pores with the direction of the arrow.

Bottom: Resultant density profile for methane along the length of simulation box in the X direction.

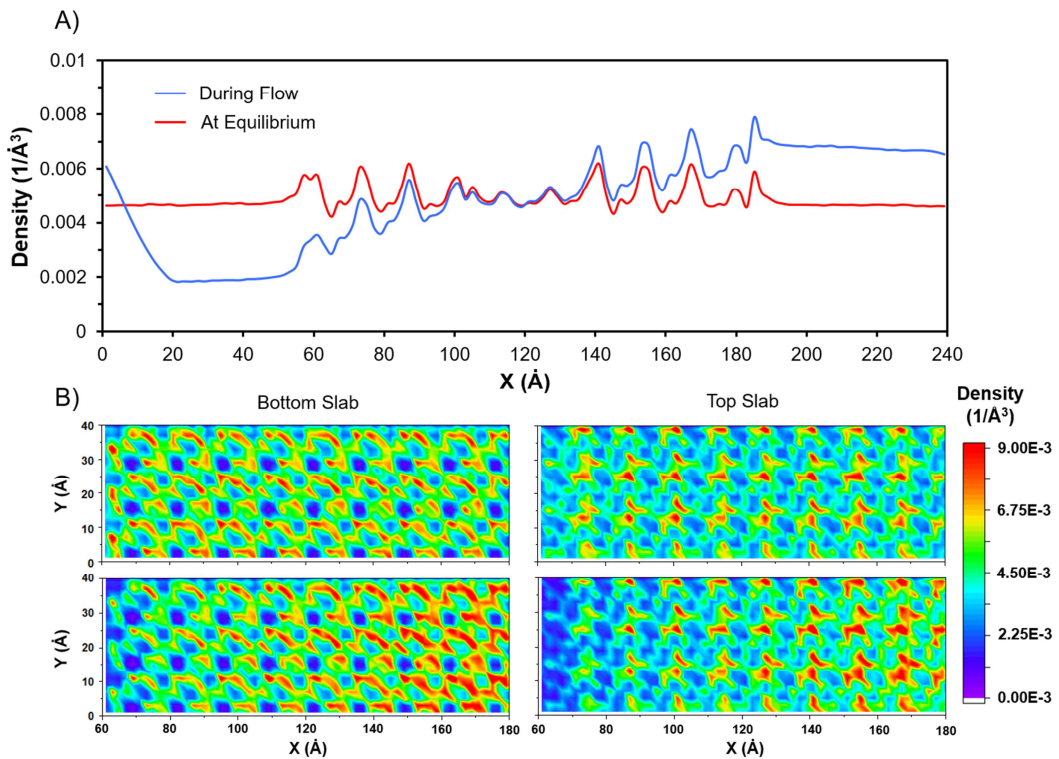


Figure 3. A) Resultant density profile of methane along the length of simulation box in the X direction when the applied force is 0.05 kcal/mol. \AA and when no force is applied. B) In-plane surface density distributions of methane molecules found in layers closest to the bottom (left panels) and top (right panels) silica slabs at equilibrium (top) and during flow (bottom). Results were obtained for system 1.

Flow Density and Velocity Vector Map. In **Figure 4** we present the density distributions obtained for methane flowing through three hierarchical pores. The projections are obtained along the X - Z plane, and super-imposed to the velocity profiles. The high-density areas (highlighted as red-yellow spots in the online version of this article) of the contour plots indicate the positions where the methane molecules preferentially accumulate. We observe that methane molecules distribute unevenly on the silica surfaces. This is due to the roughness of the amorphous silica. The methane flow develops within the network from the right (higher density) to the left (lower density). The flow is highlighted by the velocity vector field. The arrows representing the velocity vectors indicate the preferential direction of methane movement, which is in the general direction of the applied external force. However, we observe that some methane molecules near the solid surfaces move in the direction opposite to the established flow, indicating local back flows. Regions with local backflow

are commonly found within porous media when laminar flow conditions are established at the macroscale, as well as in synthetic graphene bilayers at the nanoscale [56, 57]. It is possible that these effects are due to surface roughness, which perturbs the uniform movement of fluid molecules and increases the resistance to transport. Indeed, the analysis of the percentage R of the methane molecules that move in the direction opposite to the established flow as a function of surface area (results shown in **Figure S2** in the SI) reveals that the resistance to flow scales with the surface area for some of the pore models considered here. This suggests that roughness contributes to resistance, as expected. These observations are consistent with results from Xu et al. [58], who studied the effect of wall roughness on fluid transport in carbon nanotubes and demonstrated that the transport resistance increases as the roughness increases. However, we notice that the resistance to flow in our simulations does not in general scale with surface area. The presence of bottlenecks (systems 3 and 8) and reduction of channel cross-sectional area, quantified by the entropy potential distributions (discussed below), seem to play a more important role in controlling the local backflow.

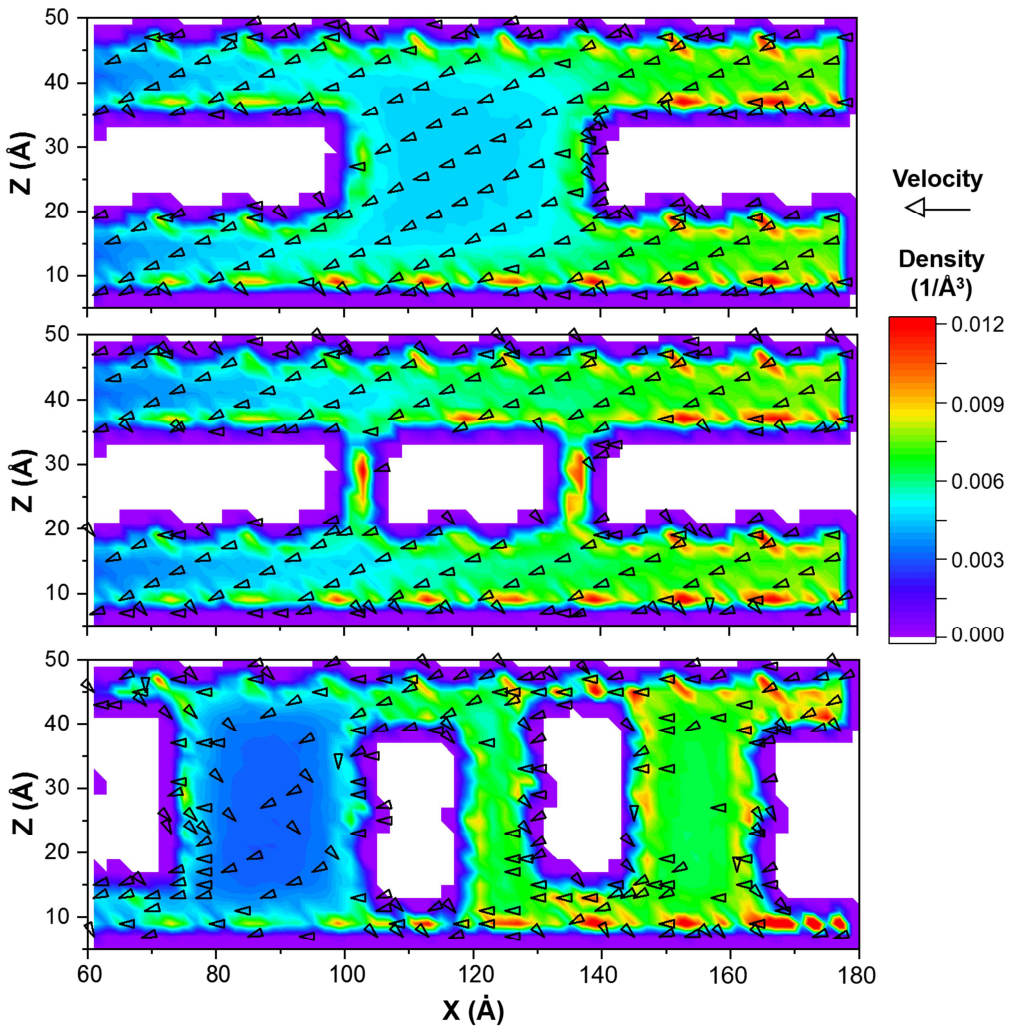


Figure 4. Surface density distributions and velocity profiles of methane flow through three representative hierarchical pores along the X-Z plane. Densities are expressed in $1/\text{\AA}^3$. Arrows represent directions of flow. It should be noted that, in our representation, the velocity field only highlights the direction of the velocity, not its magnitude.

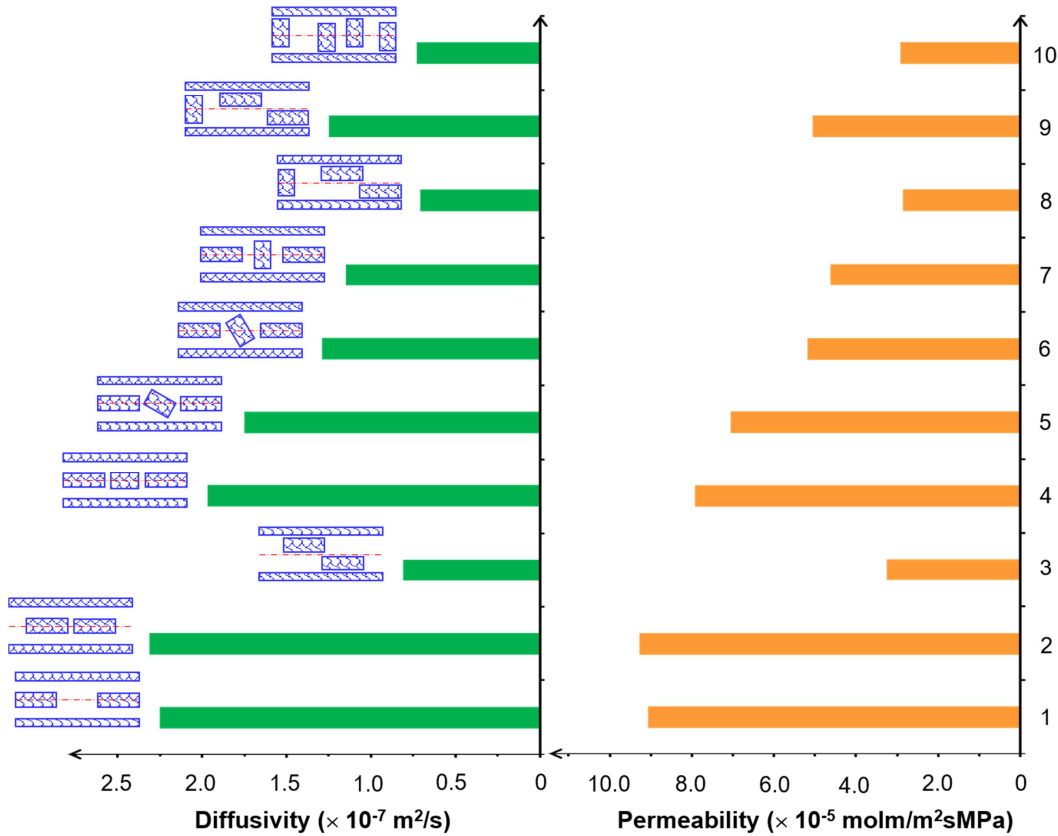


Figure 5. Effective diffusivity (left) and permeability (right) as determined by BD-NEMD simulations for methane across the ten porous model systems considered in this study.

Transport Properties. Transport diffusivities were estimated from the density gradient and molar flux, which were quantified by fitting steady-state simulation results to the Fick's first law [31]:

$$J_t = -D_t \frac{d\rho}{dx} \quad (1)$$

In most cases, both convective (pressure-driven) and diffusive (chemical potential gradient) contributions contribute simultaneously to the total flux, which could therefore be described as the sum of a convective flux and a diffusive flux. At the macroscale, the phenomenological transport coefficient D_t is therefore assumed to incorporate both diffusion and advection (convection) contributions [59, 60]. On the other hand, several computational studies [22, 28, 43, 61], which focus on the fluid transport across porous materials at the microscale, describe the transport coefficient D_t of Eq. (1) as an effective diffusivity, including both diffusive and convective contributions. In the limit of a fading pressure-driven scenario (no convective flux) such as the case considered here, the parameter D_t in Eq. (1) is expected to approach the transport diffusivity [28].

We characterized methane transport across porous media of varying cross-section channels oriented in the direction of the fluid transport. Once steady states are achieved, we obtain constant flow rates through the pore networks. The molar flux J_t is calculated as the ratio of the constant flow rate Q and the cross-section area of a channel at a given x location, $A(x)$. By substituting the molar flux J_t with the ratio of the constant flow rate Q and the cross-sectional area of a channel $A(x)$ along the X axis, we rearrange Eq. (1) and then integrate it to obtain effective diffusivities:

$$D_e = \frac{Q}{\Delta\rho} \int_0^L \frac{dx}{A(x)} \quad (2)$$

Density gradients are determined based on the molar density of fluid molecules at the inlet and outlet outside the porous medium, as shown in **Figure 2**, bottom panel. The time-averaged molar flow rate is defined as the corresponding average ensemble velocity multiplied by the system density in the X direction and the cross-sectional area of the bulk section [28, 31].

Permeabilities can be determined based on Darcy's law [62], which shows a linear relationship between molar flux and pressure drop across a porous medium. The pressure drop is calculated using the Peng-Robinson equation of states based on the molecular density of methane in feed and permeate regions as inputs [24]. Similar to the apparent diffusivity calculation described above, the permeability of methane through a porous medium can be estimated as:

$$K_e = \frac{Q}{\Delta P} \int_0^L \frac{dx}{A(x)} \quad (3)$$

By applying Eq. (2) and Eq. (3) to our simulation results, we quantify how pressure drop, flow rate and effective diffusivity depend on the applied external force. It is expected that the effective diffusivity approaches the transport diffusivity D_t in the limit of the external force going to zero. In **Figure S3** of the SI, we show a linear response to external applied forces in the range from 0.005 to 0.05 kcal/(mol. \AA). This analysis suggests that, for our systems, both pressure drop and flow rate increase significantly when the external force increases, while the effective diffusivity negligibly increases as the external field changes. Because, within the conditions considered, the effective diffusivity appears to be independent of the applied force, a single simulation is sufficient to estimate transport diffusivity. We conducted such simulations with an external force of 0.05 kcal/mol. \AA to

study methane flow through model porous systems belonging to Group *I*, *II* and *III*. The resultant pressure drops for all model systems are within the range of $\sim 20 - 22$ MPa. This is consistent with expected pressure gradients during shale gas production [63].

In **Figure 5**, the diffusivities (left panel) and permeabilities (right panel) obtained from our simulations are shown for methane transport across ten porous model systems. The results show that methane diffuses and permeates through system 3 much more slowly than through systems 1 and 2 in Group *I*. The diffusivity for methane in system 3 (0.81×10^{-7} m²/s) is ~ 3 times smaller compared to that obtained for systems 1 and 2 (2.25 and 2.31×10^{-7} m²/s, respectively). Similar results were obtained for methane permeability in systems 1 and 2 (9.07×10^{-5} and 9.28×10^{-5} molm/m²sMPa, respectively), which is higher than that obtained for system 3 (3.24×10^{-5} molm/m²sMPa). These differences could be due to the presence of a steric hindrance for fluid transport in system 3.

Inserting one small block B between two blocks A, which converts system 1 to system 4, slows down diffusion and permeation of methane through the porous medium. The diffusivity and permeability of methane through system 4 (1.97×10^{-7} m²/s and 7.92×10^{-5} molm/m²sMPa, respectively) are smaller than those for system 1 (2.25×10^{-7} m²/s and 9.07×10^{-5} molm/m²sMPa). Rotating the block B by an angle of 30° (system 5), 60° (system 6) and 90° (system 7) lessens methane diffusion and permeation (the values of effective diffusivity and permeability of methane through all pore models systems are summarized in **Table S1** of the SI).

Changing the location of two blocks A and one block B (converting system 7 to system 8), we observed remarkable changes in the methane transport through the pores. The diffusivity and permeability of methane through system 8 decrease significantly compared to those obtained for system 7. These results are likely due to the fact that the two blocks A are placed very close to each other, resulting in a bottleneck, similar to what was observed for system 3. In fact, slightly increasing the gap between the two blocks A (converting system 8 to system 9) increases methane transport rate.

The diffusivity and permeability of methane through system 9 (1.25×10^{-7} m²/s and 5.05×10^{-5} molm/m²sMPa, respectively) are slightly greater than those obtained in system 7 (1.15×10^{-7} m²/s and 4.62×10^{-5} molm/m²sMPa), although both systems have the same porosity. This difference is probably

due to the fact that system 9 is mostly composed of mesopores (76.5% of the pore volume) while system 7 is predominantly composed of micropores (89.1% of the pore volume) (we report the percentage of microporous and mesoporous volumes for all pore model systems in **Table S2** in the SI). The methane diffusion and permeation through system 10 are rather slow and comparable to those found for system 8, despite the fact that there is no bottleneck in system 10. Placing all the blocks B vertically seems to hinder fluid transport, possibly because the contact surface area of the solid substrates with fluid molecules increases. As the local back flows are found near the surfaces (as shown in **Figure 4**), the increase in the contact surface area leads to a disturbance in the uniform movement of fluid molecules, and hence diffusion and permeation of methane diminish. However, the presence of multiple small nanopores (0.4 – 0.6 nm as shown in Figure 1B, bottom panel) in system 10 is more likely to control the local backflow, as discussed above. It is worth pointing out that the simulated methane permeability through hierarchical amorphous silica porous materials considered in this study (ranging from ~ 3 to 10×10^{-5} molm/m²sMPa) is quantitatively comparable to experimental data for methane permeation through amorphous silica membranes extrapolated at 338 K reported by Kanezashi et al.[64] (permeation of $\sim 10 \times 10^{-5}$ mol/m²sMPa = $\sim 10 \times 10^{-5}$ molm/m²sMPa per one meter of amorphous SiO₂ materials). For completeness, we point out that Kanezashi et al. [64] studied small gases permeance through amorphous silica membranes consisting of a separation layer and an intermediate silica layer, which was formed by colloidal silica sols coated on the outer surface of a glass porous support. The SiO₂ separation layer was found to play a main role in controlling fluid transport rate because of the presence of nanopores of size ~ 0.385 nm.

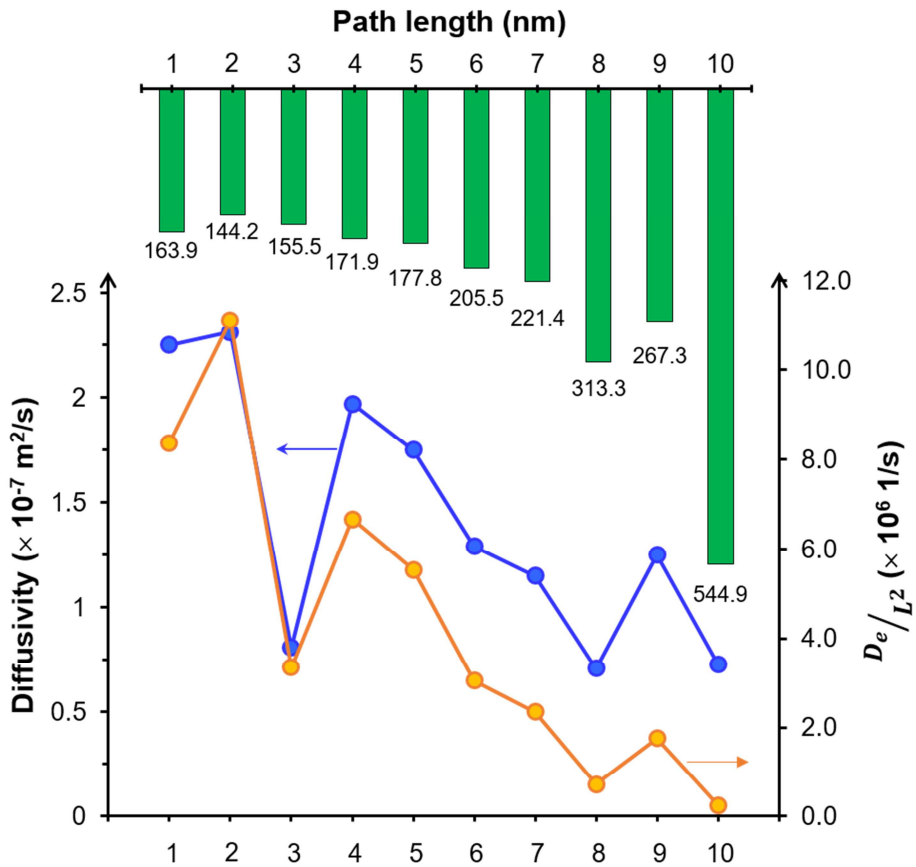


Figure 6. Effective diffusivity D_e , path length L and the inverse residence time $\nu = D_e/L^2$ of methane molecules through all pore models considered in this study.

Molecular Transport Mechanism: Path Length. To understand how methane molecules move through a porous medium, we calculated their walking path length in the X - Z plane starting from the right to the left side of the pore network. Details about path length calculations are reported in the SI (see **Figure S4** and **S5**). We computed the inverse residence time of methane within the pores by dividing the effective diffusivity by the square of path length. We report the results of path length and the inverse residence time of methane for all pore model systems, together with effective diffusivities, in **Figure 6**. The results show that, in general, the shorter the walking path length is, the larger the inverse residence time is expected to be. This observation is consistent for results obtained, in order, for system 2, 1, 4, 5, 6, 7, 8, and 10. We notice that the path length of methane walking through system 3 (155.5 nm) is shorter than the one obtained for systems 1, 4, and 5 (163.9, 171.9 and 177.8 nm, respectively) though it takes longer time for methane in system 3 to move across the pore network (i.e., $\nu = D_e/L^2$ is smaller). This result is probably due to the presence of blockage in system 3,

which hinders methane movement; however, once it passes over the bottleneck, methane ‘walks’ a shorter distance in the mesoporous channel to reach the exit. Note that systems 1, 4 or 5 consist of both micropores and mesopores, possibly leading to longer walks though the networks.

Another exception is observed in system 9, in which, despite the longer walking path length and longer residence time compared to those found for system 7 (221.4 nm), both methane diffusivity and permeability are faster. This suggests that methane would travel more easily in porous media with no blockage where larger amounts of mesoporous volume is available (i.e., 76.5% of the pore volume in system 9 is mesopores) than that of micropores (i.e., the pore volume in systems 6 and 7 is composed of 89.5% and 89.1% micropores, respectively) even though it travels a longer distance. This finding is consistent with experimental results for the diffusion of cyclohexane in hierarchical porous materials SBA-15 8.5 nm and 3DOm-i silicalite-1 using zero length column chromatography at 343 K [65]. These experimental results indicate that, although cyclohexane diffuses faster in SBA-15 than in 3DOm-i silicalite-1, the apparent diffusion lengths in SBA-15 are longer.

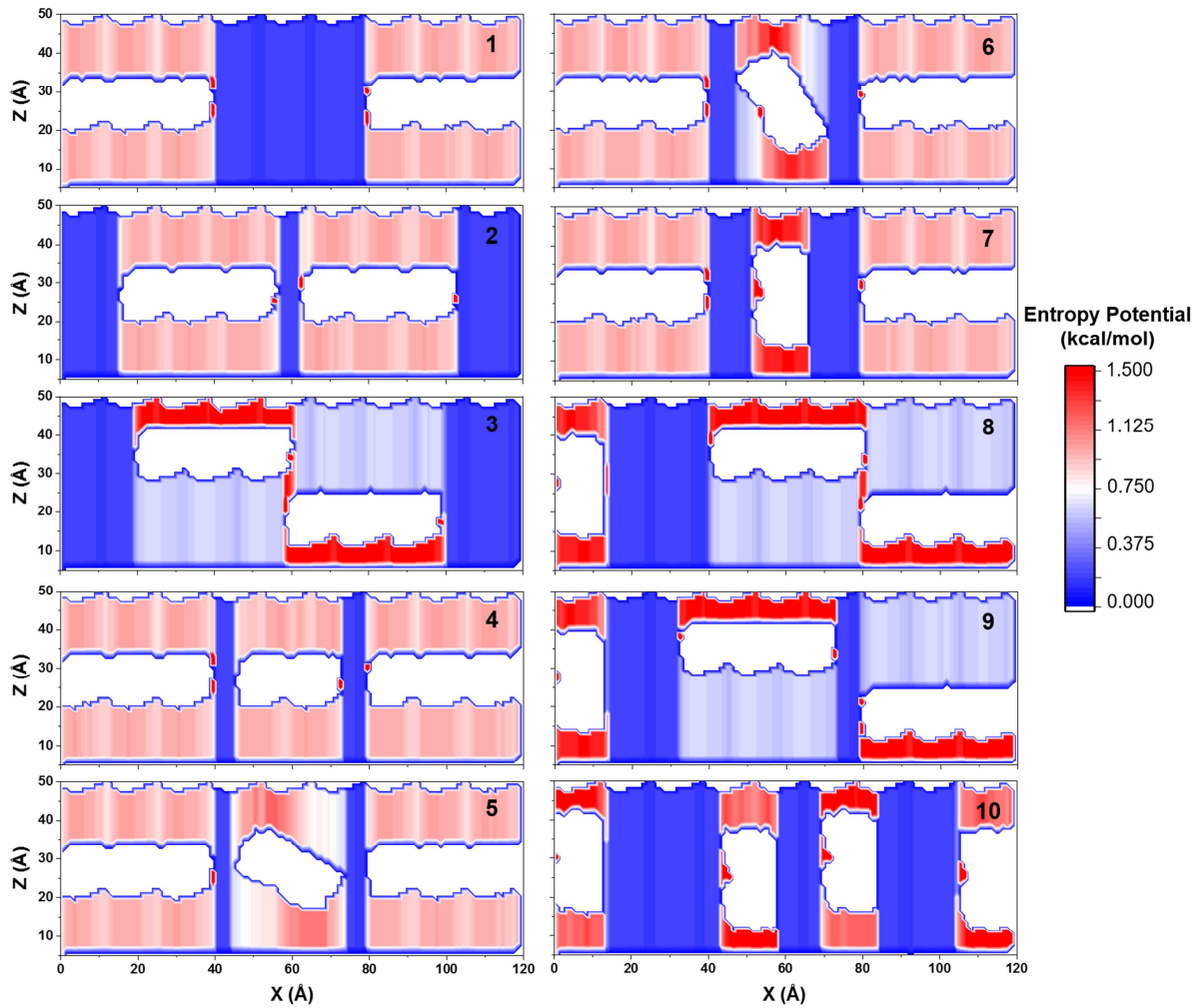


Figure 7. Entropy potential distributions on the X - Z plane for methane moving across hierarchical amorphous silica porous media. Results were obtained for the hierarchical pore model systems 1-10.

Entropy Potential Profiles. Fluid transport in narrow and tortuous pore networks, e.g., shale matrices, could be affected by the fluid molecules proceeding through obstacles and surface irregularities. An efficient approach to quantify these effects within a transport model is the quantification of entropic barriers [66]. The fluid flows considered here develop along hierarchical porous media whose cross section in the X direction varies. Following Fick and Jacobs, diffusion in porous media of varying cross section can be considered as a one-dimensional diffusion problem across entropy barriers due to changes in channel cross-sectional area [67]. Within this scenario, the entropy potential $U(x)$ can be defined as [67, 68]

$$U(x) = -k_B T \ln \frac{A(x)}{A(x_0)} \quad (4)$$

In Eq. (4), $A(x)$ is the cross-section area of a channel at position x . For reference, $U(x)$ at $x = x_0$ is taken to be zero when we consider $A(x_0)$ as the cross-section area of the bulk section, outside the pore networks. k_B and T in Eq. (4) are the Boltzmann constant and the absolute temperature, respectively.

The entropic barriers likely affect the travel path length, and therefore could play a crucial role in controlling fluid transport. We quantified the in-plane entropy potential distribution across all hierarchical pore models considered. The results are presented in **Figure 7**. The high-entropy areas (red spots) of the contour plot indicate the positions where fluid molecules encounter strong resistance to transport. The results show that methane molecules flowing through systems 3 and 8 experience strong hindrance, with large entropic barriers of 1.96 and 1.76 kcal/mol, respectively. Consequently, the transport diffusion and permeability of methane in both systems 3 and 8 are much smaller compared to those in other systems. We observe that as the block B rotates about its center (systems 4, 5, 6, and 7), the entropic barriers range from 1.03 to 1.61 kcal/mol, slowing down both transport diffusion and permeation. The results show, as expected, that the extremely large entropic barrier between two blocks A in system 8 vanishes when block A is shifted slightly further away from the other block A (convert system 8 to 9). This enhances the rate of methane transport for system 9. More mesopores are found in system 9 than in system 7 (see **Table S2** of the SI), as quantified by smaller entropy potentials; this results in larger methane transport diffusion and permeation in system 9. The results of entropy potential distribution for system 10 show that the travelling path of methane molecules are likely to be more tortuous due to the zigzag arrangement of strong entropic barriers, which impedes methane tranport rate. This observation is confirmed by the analysis of path length for methane moving across the pore model system 10 (see **Table S1** of the SI).

Relation between Transport Properties and Pore Characteristics. The most common representation of the diffusion coefficient of a given fluid within a porous medium, D_m , relative to the diffusion coefficient of the same fluid in the bulk, D_{bulk} , is given in terms of porosity ϕ_m , tortuosity τ_m and constriction factor C_m [38, 43]:

$$D_m = D_{bulk} \frac{\phi_m}{\tau_m \cdot C_m} \quad (5)$$

This approach is consistent with several contributions from the literature [4, 35, 39, 69]. For example, Kärger and co-workers indicated that the fluid diffusivity in a porous solid, D , could be related to its diffusivity, under equivalent physical conditions, in a straight cylindrical pore, D_p , with diameter equal to the mean pore diameter in the porous material, by the following relation [43]:

$$D = D_p \frac{\phi}{\tau_c} \quad (6)$$

Similarly, we attempt here to relate the effective diffusivity of methane, D_e , through a pore model to its effective diffusivity, D_0 , through the reference pore model, which consists of a slit-shaped pore obtained by two parallel silica slabs (system 0, see **Figure S1** of the SI). Relative porosity ϕ , constriction factor C , and tortuosity τ are calculated as the ratio of the parameters quantified in a pore network to those quantified for the reference, system 0 ($\phi = \phi_i / \phi_0$, $C = C_i / C_0$, and $\tau = \tau_i / \tau_0$, respectively).

The constriction factor C_i for a porous medium of length L with varying cross-sectional area $A(x)$ along the direction of transport x , is determined as [70]:

$$C_i = \frac{1}{L^2} \int_0^L A(x)^2 dx \int_0^L \frac{1}{A(x)^2} dx \quad (7)$$

The diffusive tortuosity is considered in this study, and it is calculated as [71]:

$$\tau_i = \left(\frac{L_i}{L_0} \right)^2 \quad (8)$$

In Eq. (8), L_i is the walking path length of methane within system i (values are reported in **Table S1**). We report the relative porosity, constriction factor and tortuosity for methane transport through all pore model systems considered in this study in **Table S3** of the SI.

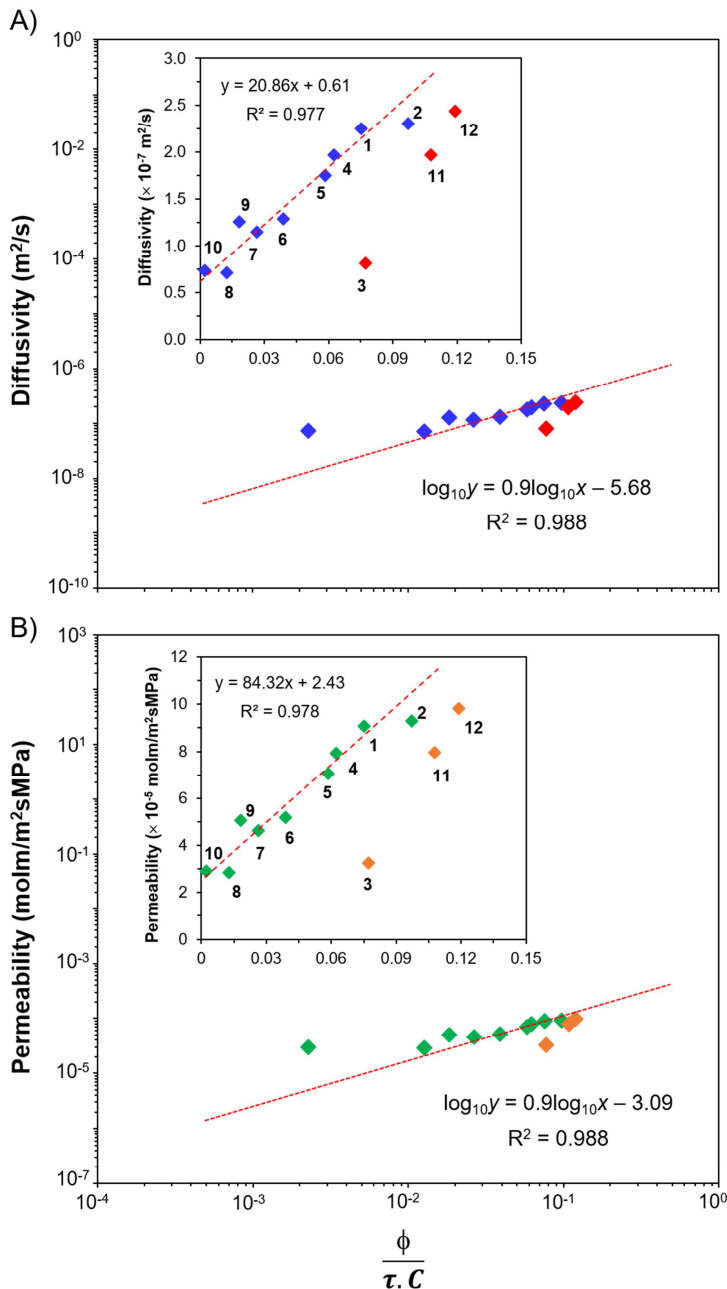


Figure 8. Methane effective diffusivity (panel A) and permeability (panel B) as function of the pore characteristic parameter defined by the ratio of porosity to tortuosity and constriction factor on logarithmic plots. In both panels, the insets provide representations for the data on Cartesian plots. Results were obtained for all hierarchical pore model systems considered in this work.

In **Figure 8**, we show the results of effective diffusivity and permeability of methane for all pore models as a function of the pore characteristic parameter $\phi/(\tau \cdot C)$ on logarithmic plots (main) and Cartesian plots (insets). We observe a linear relation on both logarithmic and Cartesian plots. When the data are displayed on the logarithmic plots, a linear fit clearly shows that the effective diffusivity

(/permeability) of methane converges closely to zero as the pore characteristic parameter $\phi/(\tau C)$ approaches zero.

It is noted that the slope of the linear function for the effective diffusivity (/permeability) and pore characteristic parameter ($20.86 \times 10^{-7} \text{ m}^2/\text{s}$ (/ $84.32 \times 10^{-5} \text{ molm/m}^2\text{sMPa}$)) on the Cartesian plot are consistent with ten to the power of the intercept of the linear relation on the logarithmic plot ($20.86 \times 10^{-7} \approx 10^{-5.68} \text{ m}^2/\text{s}$ or $84.32 \times 10^{-5} \approx 10^{-3.09} \text{ molm/m}^2\text{sMPa}$). These values are related to the effective diffusivity (/permeability) of methane through the reference system 0 [$20.6 \times 10^{-7} \text{ m}^2/\text{s}$ (/ $83.2 \times 10^{-5} \text{ molm/m}^2\text{sMPa}$), see **Table S1** of the SI]. This means that the expression for the diffusivity of fluid through a pore model versus the pore characteristic parameter ($D_e = D_0 \times \phi/(\tau C) + \text{const.}$) complies with the macroscopic relations described by Eq. (6).

It is also observed that the relation between methane transport and pore characteristic parameter for system 3 does not follow the linear trend found for all other systems. This is particularly evident on the Cartesian plot. The difference between the pore network represented by system 3 and the others is that only mesopores ($> 2\text{nm}$) are found in system 3. We speculate that the linear correlation between the transport properties and the pore characteristic parameter shown in **Figure 8** holds for hierarchical porous materials that include both mesopores and microspores, but not for those with only mesopores. To confirm this presumption, we build two additional model systems, 11 and 12, which contain only mesopores with no pore blockage (schematics for systems 11 and 12 are shown in **Figure S1** of the SI). When the methane transport properties are compared to the network pore characteristics, we observe that the linear trend discussed in **Figure 8** is not followed, similarly to results just discussed for system 3. As discussed above, because of the presence of a bottleneck, the effective diffusivity in system 3 is much smaller compared to that obtained in other systems with similar porosity. However, once methane passes through the bottleneck, it travels a shorter distance, in the mesopore, to exit the material, resulting in small diffusive tortuosity; as a consequence, $\phi/\tau C$ is large. For systems 11 and 12, within which the bottleneck gradually disappears, the methane diffusivity increases significantly, as can be appreciated by the results obtained for system 12, faster compared to all other systems considered. Note that in these systems methane ‘walks’ even a much

shorter distance in the mesopore to reach the exit due to small resistance to the flow, and as a result of this $\phi/\tau \cdot C$ becomes larger. This results in the positions of these red symbols in the insets of Figure 8, panel A.

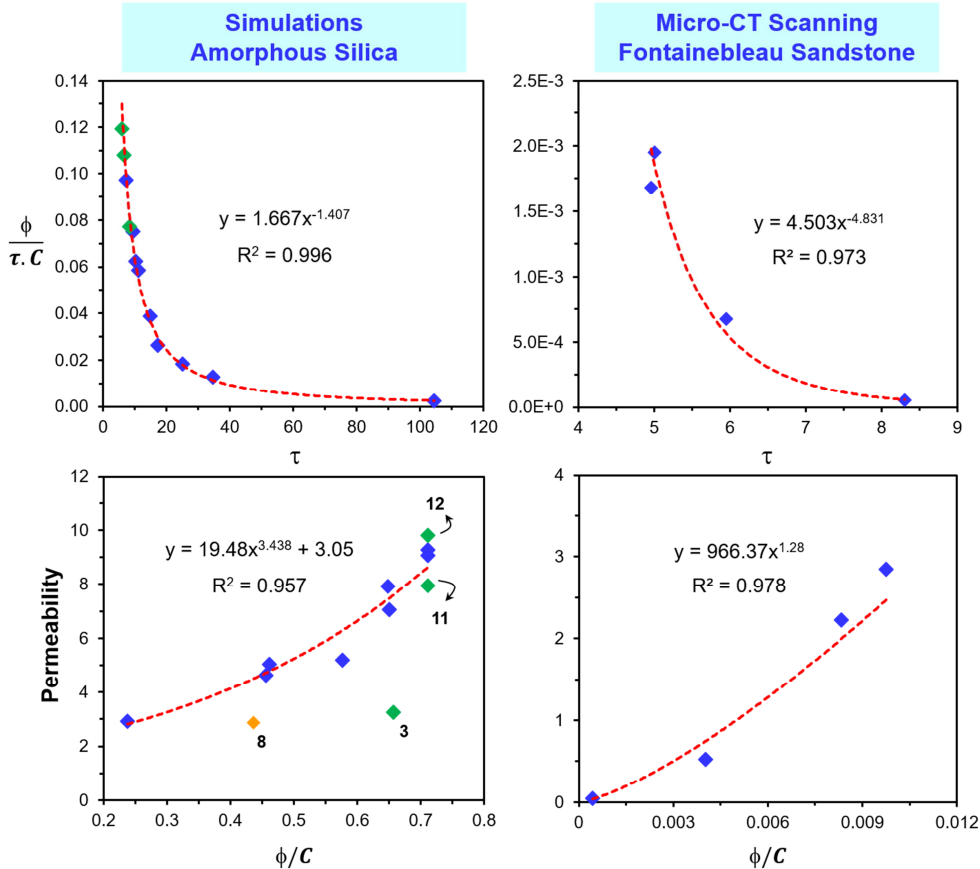


Figure 9. Top panels: Relation between porosity, constriction factor and tortuosity. Bottom panels: Correlation between permeability and the ratio of porosity to constriction factor. The results from the simulations for hierarchical amorphous silica porous materials in this study, and those from micro-CT scan [70, 72] and experiments [73, 74] for the Fontainebleau sandstone are shown in left and right panels, respectively.

Predictive Models. The availability of reliable transport properties measured/simulated across pore networks that are described accurately by precise geometrical features allows us to attempt answering the long-standing quest of predicting transport properties through a pore network. Before embarking on this investigation, it should be noted that the definition of tortuosity employed in our work is based on the average length of flow paths in the direction of flux, i.e., the diffusive tortuosity, and therefore depends on the microscopic pore geometry, as well as on the transport mechanism under examination [75].

We seek a relationship between fluid transport properties and measurable descriptors of pore structure, *i.e.*, porosity and constriction factor, without using tortuosity.

We recall that methane permeability (/diffusivity) was found to depend linearly on the pore characteristic parameter $\phi/(\tau.C)$ (see **Figure 8**). Plotting the pore characteristic parameter $\phi/(\tau.C)$ versus tortuosity τ for the hierarchical porous materials, we observe the power relationship (**Figure 9**, top left panel) described as:

$$\frac{\phi}{\tau.C} = a\tau^{-\beta} \quad (9)$$

Substituting Eq. (9) within the linear relation between permeability (/diffusivity) and pore characteristic parameter $\phi/(\tau.C)$, we suggest that the fluid permeability (/diffusivity) correlates with the measurable pore descriptor ϕ/C , via the function:

$$K = \frac{K_0}{a^{1/(\beta-1)}} \left(\frac{\phi}{C} \right)^{\frac{\beta}{\beta-1}} + const. \quad (10)$$

$$D = \frac{D_0}{a^{1/(\beta-1)}} \left(\frac{\phi}{C} \right)^{\frac{\beta}{\beta-1}} + const. \quad (11)$$

In **Figure 9**, bottom left panel, we plot methane permeability versus ϕ/C for amorphous silica pores, showing that $\beta/(\beta-1) \sim 3.44$ and that $K_0/a^{1/(\beta-1)} \sim 19.48$ when $K_0 = 84.32$ (as obtained from **Figure 8**, panel B), $a = 1.667$ and $\beta = 1.407$ (as obtained from **Figure 9**, top left panel).

The permeability of methane through systems containing strong blockages [systems 3 (green) or 8 (yellow)] does not obey Eq. (9) (**Figure 9**, bottom left panel). However, transport properties obtained in model systems 11 and 12 (green data points) seem to be well fitted. This agreement could be spurious, because the results for these systems deviate from the trends discussed in **Figure 8**. Hence, we recommend not using results from systems 11 and 12 to obtain the power parameters in Eq. (9) [75]. In fact, we consider the relation shown in Eq. (9) a useful model for porous media that contain both micropores and mesopores and do not show strong pore blockages.

As a final test, we apply the model of Eq. (9) to natural porous media. Berg [70] reported pore structure parameters such as characteristic length, constriction factor, porosity and tortuosity for Fontainebleau sandstone, as obtained from experimental microtomographic (micro-CT) images. Arns et al. [72] conducted numerical micropermeametry calculations on three-dimensional digitized images

of Fontainebleau sandstone and obtained results in good agreement with experiments [73, 74] over a wide range of porosities. This system offers a benchmark for testing the capability of Eq. (10).

In **Figure 9**, right panels, we present the relation between pore characteristic parameter $\phi/(\tau.C)$ and tortuosity τ (top), and that between permeability and parameter ϕ/C (bottom) for Fontainebleau sandstone data. We observe that $\phi/(\tau.C)$ decreases with tortuosity following a power function with exponent $\beta = 4.831$ and parameter $a = 4.503$ (**Figure 9**, top right panel). Note that the relation between permeability and pore characteristic parameter $\phi/(\tau.C)$ is also linear with slope $K_0 \sim 1498.8$ (**Figure S6** of the SI). In **Figure 9**, bottom right panel, it is shown that the fluid permeability increases with ϕ/C following a power function with exponent 1.28 and parameter of 966.37, which are equivalent to $\beta/(\beta-1)$ and $K_0/a^{1/(\beta-1)}$, respectively, in Eq. (10).

The results just described suggest that the empirical Eq. (10) could be used to predict the permeability (or effective diffusivity) of fluids through various sedimentary rocks once detailed rock structure information, e.g. porosity and constriction factor are known. When applied to our simulation results for methane transport in silica-based pore networks containing both mesopores and micropores, it was found that K_0 , a and β assumed the values of 84.32, 1.667 and 1.407, respectively. It is expected that these values, and in particular the exponent $\beta/(\beta-1)$ and the parameter $K_0/a^{1/(\beta-1)}$, will change with different types of fluids as well as different types of porous media.

4. Conclusions

This study presents an atomistic modelling of methane transport through hierarchical amorphous silica porous materials at 338K, obtained by using boundary-driven non-equilibrium molecular dynamics (BD-NEMD) simulations. The NEMD approach closely resembles how experiments are carried out to measure gas permeation through porous materials, yielding a macroscopic view of natural gas transport in porous media such as shale matrices. Our results show that the pore structure has a major impact on methane transport through hierarchical porous networks. For example, changing contact surface areas between the amorphous SiO₂ substrates and methane perturbs methane diffusion and permeation, because of the introduction of local back flow near the surfaces. In addition,

changes in entropy potentials along the direction of flow due to varying pore cross-sectional areas substantially alter the traveling path length of molecules. We demonstrated how the transport properties of methane correlate with macroscopic descriptors of the pore structure and we derived an empirical expression for diffusivity and permeability of fluid through hierarchical porous materials as a power function of such measurable descriptors. This study suggests that an atomistic modelling approach based on BD-NEMD simulations can be used to predict fluid transport properties across sedimentary rocks through an empirical power relation. Bridging the gaps between the results obtained within a few pores, a few hundreds of pores, and ultimately within complex pore networks requires the development of bottom-up multiscale modelling frameworks, perhaps synergistically with predictive empirical relations. Numerous computational and theoretical approaches such as coarse-grained molecular dynamics simulations [76, 77], Lattice Boltzmann Method [78, 79], and Kinetic Monte Carlo simulations [19, 80] have been attempted, each with both promising features and drawbacks, to access longer length and time scales while accounting for fluid-rock interactions and the wide range of confined fluid states.

Acknowledgments

Generous allocations of computing time were provided by the University College London Research Computing Platforms Support (LEGION), the Oklahoma Supercomputing Center for Education and Research (OSKER) and the National Energy Research Scientific Computing Center (NERSC) at Lawrence Berkeley National Laboratory. NERSC is supported by the DOE Office of Science under Contract No. DE-AC02-05CH11231. This work is a part of the Science4CleanEnergy European research consortium funded by European Union’s Horizon 2020 research and innovation programme, under grant agreement No. 764810 (S4CE). We are grateful to Prof. John Shaw for insightful discussions. Prof. Shaw’s sabbatical at University College London was in part supported by the Leverhulme Trust under grant agreement number VP2-2017-023.

Appendix A. Supporting Information

Details about hierarchical pore model constructions and their geometries as well as walking path length calculations. Results for (1) Percentage R of the number of methane molecules that move in the direction opposite to the established flow and contact surface areas (2) linear response behaviour of pressure drop, flow rate and apparent diffusivity activated by various applied external fields; (3) probability distributions of path length walks for methane crossing a pore network; (4) relation between permeability and pore characteristics for Fontainebleau sandstone; (5) Effective diffusivity, permeability, path length and inverse residence time of methane through each system; (6) percentage of microporous and mesoporous volumes for systems 1 – 10; and (7) Relative porosity, constriction factor and tortuosity for systems 1 – 10.

References

- [1] A. Striolo, D.R. Cole, *Energ Fuel*, 31 (2017) 10300-10310.
- [2] L. Ma, A.L. Fauchille, P.J. Dowey, F.F. Pilz, L. Courtois, K.G. Taylor, P.D. Lee, *Geol Soc Spec Publ*, 454 (2017) 175-199.
- [3] J.J. Wang, L. Chen, Q.J. Kang, S.S. Rahman, *Fuel*, 181 (2016) 478-490.
- [4] S.J. Reich, A. Svidrytski, D. Hluskou, D. Stoeckel, C. Kubel, A. Holtzel, U. Tallarek, *Ind Eng Chem Res*, 57 (2018) 3031-3042.
- [5] S.J. Reich, A. Svidrytski, A. Holtzel, J. Florek, F. Kleitz, W. Wang, C. Kubel, D. Hluskou, U. Tallarek, *J Phys Chem C*, 122 (2018) 12350-12361.
- [6] T. Mullner, K.K. Unger, U. Tallarek, *New J Chem*, 40 (2016) 3993-4015.
- [7] A. Ledesma-Duran, S.I.H. Hernandez, I. Santamaria-Holek, *J Phys Chem C*, 120 (2016) 29153-29161.
- [8] B. Coasne, A. Galarneau, C. Gerardin, F. Fajula, F. Villemot, *Langmuir*, 29 (2013) 7864-7875.
- [9] A. Galarneau, F. Villemot, J. Rodriguez, F. Fajula, B. Coasne, *Langmuir*, 30 (2014) 13266-13274.
- [10] K. Falk, B. Coasne, R. Pellenq, F.J. Ulm, L. Bocquet, *Nat Commun*, 6 (2015).
- [11] T. Le, A. Striolo, D.R. Cole, *J Phys Chem C*, 119 (2015) 15274-15284.
- [12] N.R. Backeberg, F. Iacoviello, M. Rittner, T.M. Mitchell, A.P. Jones, R. Day, J. Wheeler, P.R. Shearing, P. Vermeesch, A. Striolo, *Sci Rep-Uk*, 7 (2017).
- [13] A.R. Bhandari, P.B. Flemings, P.J. Polito, M.B. Cronin, S.L. Bryant, *Transport Porous Med*, 108 (2015) 393-411.
- [14] G.R.L. Chalmers, D.J.K. Ross, R.M. Bustin, *Int J Coal Geol*, 103 (2012) 120-131.
- [15] Y.M. Metwally, C.H. Sondergeld, *International Journal of Rock Mechanics and Mining Sciences*, 48 (2011) 1135-1144.
- [16] S. Succi, *Phys Rev Lett*, 89 (2002).
- [17] J.L. Zhao, J. Yao, M. Zhang, L. Zhang, Y.F. Yang, H. Sun, S.Y. An, A.F. Li, *Sci Rep-Uk*, 6 (2016).
- [18] L. Chen, Q.J. Kang, H.S. Viswanathan, W.Q. Tao, *Water Resour Res*, 50 (2014) 9343-9365.
- [19] M. Apostolopoulou, R. Day, R. Hull, M. Stamatakis, A. Striolo, *J Chem Phys*, 147 (2017).
- [20] P. Tahmasebi, F. Javadpour, M. Sahimi, *Int J Coal Geol*, 165 (2016) 231-242.
- [21] Z.H. Jin, A. Firoozabadi, *J Chem Phys*, 143 (2015).
- [22] E.J. Maginn, A.T. Bell, D.N. Theodorou, *J Phys Chem-Us*, 97 (1993) 4173-4181.
- [23] T.A. Ho, A. Striolo, *Aiche J*, 61 (2015) 2993-2999.
- [24] A. Phan, D.R. Cole, R.G. Weiss, J. Dzubiella, A. Striolo, *Acs Nano*, 10 (2016) 7646-7656.
- [25] T. Bui, A. Phan, D.R. Cole, A. Striolo, *J Phys Chem C*, 121 (2017) 15675-15686.
- [26] F.Q. Zhu, E. Tajkhorshid, K. Schulten, *Biophys J*, 83 (2002) 154-160.

- [27] A. Ozcan, C. Perego, M. Salvalaglio, M. Parrinello, O. Yazaydin, *Chem Sci*, 8 (2017) 3858-3865.
- [28] H. Frentrup, C. Avendano, M. Horsch, A. Salih, E.A. Muller, *Mol Simulat*, 38 (2012) 540-553.
- [29] Z. Hato, A. Kaviczki, T. Kristof, *Mol Simulat*, 42 (2016) 71-80.
- [30] C. Berti, S. Furini, D. Gillespie, *J Chem Theory Comput*, 12 (2016) 925-929.
- [31] S. He, J.C. Palmer, G. Qin, *Micropor Mesopor Mat*, 249 (2017) 88-96.
- [32] H.S. Fogler, *Elements of Chemical Reaction Engineering*, Prentice-Hall International, London, 1999.
- [33] F.A. Coutelieris, J.M. Delgado, *Transport Processes in Porous Media*, Springer Science & Business Media, Heidelberg, 2012.
- [34] D. Hlushkou, U. Tallarek, *J Chromatogr A*, 1581 (2018) 173-179.
- [35] J. Vanbrakel, P.M. Heertjes, *Int J Heat Mass Tran*, 17 (1974) 1093-1103.
- [36] N. Epstein, *Chem Eng Sci*, 44 (1989) 777-779.
- [37] L. Shen, Z.X. Chen, *Chem Eng Sci*, 62 (2007) 3748-3755.
- [38] B. Ghanbarian, A.G. Hunt, R.P. Ewing, M. Sahimi, *Soil Sci Soc Am J*, 77 (2013) 1461-1477.
- [39] T.B. Boving, P. Grathwohl, *J Contam Hydrol*, 53 (2001) 85-100.
- [40] P. Ugliengo, M. Sodupe, F. Musso, I.J. Bush, R. Orlando, R. Dovesi, *Adv Mater*, 20 (2008) 4579-4583.
- [41] D. Schneider, D. Mehlhorn, P. Zeigermann, J. Karger, R. Valiullin, *Chem Soc Rev*, 45 (2016) 3439-3467.
- [42] B. Coasne, *New J Chem*, 40 (2016) 4078-4094.
- [43] J. Kärger, D.M. Ruthven, D.N. Theodorou, *Diffusion in Nanoporous Materials*, John Wiley & Sons, Weinheim, 2012.
- [44] R.T. Cygan, J.J. Liang, A.G. Kalinichev, *J Phys Chem B*, 108 (2004) 1255-1266.
- [45] M.G. Martin, J.I. Siepmann, *J Phys Chem B*, 102 (1998) 2569-2577.
- [46] J.W. Eastwood, R.W. Hockney, D.N. Lawrence, *Comput Phys Commun*, 19 (1980) 215-261.
- [47] M.P. Allen, D.J. Tildesley, *Computer Simulation of Liquids*, Oxford University Press, Oxford, UK, 2004.
- [48] B. Hess, C. Kutzner, D. van der Spoel, E. Lindahl, *J Chem Theory Comput*, 4 (2008) 435-447.
- [49] D. Van der Spoel, E. Lindahl, B. Hess, G. Groenhof, A.E. Mark, H.J.C. Berendsen, *J Comput Chem*, 26 (2005) 1701-1718.
- [50] S. Plimpton, *J Comput Phys*, 117 (1995) 1-19.
- [51] R.W. Hockney, S.P. Goel, J.W. Eastwood, *J Comput Phys*, 14 (1974) 148-158.
- [52] S. Nose, *Mol Phys*, 52 (1984) 255-268.
- [53] W.G. Hoover, *Phys Rev A*, 31 (1985) 1695-1697.
- [54] S. Chempath, R. Krishna, R.Q. Snurr, *J Phys Chem B*, 108 (2004) 13481-13491.

- [55] P. Hunenberger, *Adv Polym Sci*, 173 (2005) 105-147.
- [56] D. Hlushkou, U. Tallarek, *J Chromatogr A*, 1126 (2006) 70-85.
- [57] B. Liu, R.B. Wu, A.W.K. Law, X.Q. Feng, L.C. Bai, K. Zhou, *Sci Rep-Uk*, 6 (2016).
- [58] B.X. Xu, Y.B. Li, T. Park, X. Chen, *J Chem Phys*, 135 (2011).
- [59] D. Hlushkou, S. Bruns, A. Holtzel, U. Tallarek, *Anal Chem*, 82 (2010) 7150-7159.
- [60] D. Hlushkou, S. Bruns, A. Seidel-Morgenstern, U. Tallarek, *J Sep Sci*, 34 (2011) 2026-2037.
- [61] B. Smit, T.L.M. Maesen, *Chem Rev*, 108 (2008) 4125-4184.
- [62] R.M. Roque-Malherbe, *Adsorption and Diffusion in Nanoporous Materials*, CRC Press2007.
- [63] T.A. Ho, Y.F. Wang, A. Ilgen, L.J. Criscenti, C.M. Tenney, *Nanoscale*, 10 (2018) 19957-19963.
- [64] M. Kanezashi, T. Sasaki, H. Tawarayama, H. Nagasawa, T. Yoshioka, K. Ito, T. Tsuru, *J Phys Chem C*, 118 (2014) 20323-20331.
- [65] V. Vattipalli, X.D. Qi, P.J. Dauenhauer, W. Fan, *Chem Mater*, 28 (2016) 7852-7863.
- [66] P. Malgaretti, I. Pagonabarraga, M. Rubi, *Frontiers in Physics*, 1 (2013) 21.
- [67] R. Zwanzig, *J Phys Chem-US*, 96 (1992) 3926-3930.
- [68] A.M. Berezhkovskii, M.A. Pustovoit, S.M. Bezrukov, *J Chem Phys*, 126 (2007).
- [69] C.F. Berg, *Phys Rev E*, 86 (2012).
- [70] C.F. Berg, *Transport Porous Med*, 103 (2014) 381-400.
- [71] A. Ledesma-Duran, S.I. Hernandez, I. Santamaria-Holek, *Phys Rev E*, 95 (2017).
- [72] C.H. Arns, M.A. Knackstedt, W.V. Pinczewski, N.S. Martys, *J Petrol Sci Eng*, 45 (2004) 41-46.
- [73] C.G. Jacquin, *Rev. Inst. Fr. Pet.*, 19 (1964) 921.
- [74] J.T. Fredrich, K.H. Greaves, J.W. Martin, *Int J Rock Mech Min*, 30 (1993) 691-697.
- [75] A. Koponen, M. Kataja, J. Timonen, *Phys Rev E*, 54 (1996) 406-410.
- [76] A. Vishnyakov, R. Mao, M.T. Lee, A.V. Neimark, *J Chem Phys*, 148 (2018).
- [77] K. Zhang, D. Meng, F. Muller-Plathe, S.K. Kumar, *Soft Matter*, 14 (2018) 440-447.
- [78] M. Levesque, M. Duvail, I. Pagonabarraga, D. Frenkel, B. Rotenberg, *Phys Rev E*, 88 (2013).
- [79] J.M. Vanson, F.X. Coudert, B. Rotenberg, M. Levesque, C. Tardivat, M. Klotz, A. Boutin, *Soft Matter*, 11 (2015) 6125-6133.
- [80] A. M., D. R., D. R., S. M., C. M.O., S. A., *Int J Coal Geol*, 205 (2019) 140-154.

Highlights

- Strong dependence of methane diffusivity and permeability on the features of synthetic pore frameworks.
- Existence of local back-flow near solid substrates due to surface roughness, presence of bottle necks and changes in channel areas accessible to flow, which disturbs methane transport.
- Changes in entropy potential along a flow direction strongly affect molecular path length.
- A linear relationship between methane transport and a pore characteristic parameter has been identified.
- Fluid transport properties scale as a power function based on measurable pore structure parameters.

Graphical abstract

